APPLIED PHYSICS

Spin-charge conversion in NiMnSb Heusler alloy films

Zhenchao Wen[1,2,3*†], Zhiyong Qiu[1,4†], Sebastian Tölle[5], Cosimo Gorini[6*], Takeshi Seki[1,2], Dazhi Hou[7], Takahide Kubota[1,2], Ulrich Eckern[5], Eiji Saitoh[1,7], Koki Takanashi[1,2,8]

Half-metallic Heusler alloys are attracting considerable attention because of their unique half-metallic band structures, which exhibit high spin polarization and yield huge magnetoresistance ratios. Besides serving as ferromagnetic electrodes, Heusler alloys also have the potential to host spin-charge conversion. Here, we report on the spin-charge conversion effect in the prototypical Heusler alloy NiMnSb. An unusual charge signal was observed with a sign change at low temperature, which can be manipulated by film thickness and ordering structure. It is found that the spin-charge conversion has two contributions. First, the interfacial contribution causes a negative voltage signal, which is almost constant versus temperature. The second contribution is temperature dependent because it is dominated by minority states due to thermally excited magnons in the bulk part of the film. This work provides a pathway for the manipulation of spin-charge conversion in ferromagnetic metals by interface-bulk engineering for spintronic devices.

INTRODUCTION

The spin-charge conversion in well-designed materials is essential for the development of future energy-efficient spintronic devices (*1*–*7*). Recently, spin currents generated from ferromagnets (FMs)—such as CoFeB (*8*, *9*), NiFe (*9*–*11*), and FePt (*12*)—are attracting great attention not only due to the remarkable spin signals but also due to their controllability owing to interactions between spin and magnetization. Among FMs, half-metallic FMs (HMFs) are a unique class of FMs with respect to their electronic band structure: One spin channel exhibits a band gap at the Fermi level, and the other one is conductive (*13*, *14*). This unique band structure yields a high spin polarization (ideally 100%), resulting in very high performances of HMF-based spintronic devices, such as a huge tunneling magnetoresistance ratio of more than 2000% (*15*). However, the spin-charge conversion, a basic spin-related effect, was considered to be forbidden because only one spin channel is available in the ground state of HMFs. Ohnuma *et al.* (*16*) theoretically predicted that spin-charge conversion can occur with the assistance of magnons at a finite temperature, which opens a possibility for spin-charge conversion in HMFs. Furthermore, the degradation of perfect half-metallicity in the interface/surface region (*17*–*22*) is another possibility of spin-charge conversion in these materials.

Here, we study the spin-charge conversion in a NiMnSb Heusler alloy, which was first reported to be an HMF by first-principle calculations (*13*). Figure 1A shows a schematic illustration of its crystal structure in the $C1_b$ phase. Recently, Wen *et al.* (*23*, *24*) succeeded in measuring a current-perpendicular-to-plane giant magnetoresistance with high-quality NiMnSb films. Ciccarelli *et al.* (*25*) reported on spin-orbit torques in NiMnSb at room temperature. As shown in Fig. 1B, NiMnSb has a typical half-metallic band structure where the minority spin band shows a gap at the Fermi level for the bulk state. However, the minority gap closes owing to electron-magnon interactions and interface/surface states (Fig. 1B) (*17*). Thus, the spin-charge conversion is expected because of the bulk and interface contributions, as shown in Fig. 1C.

In this work, NiMnSb films with varying thickness and ordering structure were deposited on $Y_3Fe_5O_{12}$ (YIG) substrates, the quality of which was confirmed by structural analysis and anisotropic magnetoresistance (AMR). Spin currents were injected into NiMnSb from the insulating YIG layers by spin pumping. Then, the spin currents were converted to charge currents by means of spin-orbit interactions and detected as voltage signals. An unusual temperature dependence of the voltage was observed with a sign change at low temperature, which can be controlled by the thickness and ordering structure of the NiMnSb films. The origin of the unusual voltage signals can be well interpreted by the spin-charge conversion due to interface and bulk contributions.

RESULTS

Figure 2A shows the structural properties of NiMnSb films characterized by out-of-plane x-ray diffraction (XRD). Two kinds of samples with different ordering structures were prepared on YIG substrates. One was annealed at a high temperature of 500°C, and the other, named less-ordered sample, was grown at room temperature. In addition to the diffraction peaks from YIG substrate, XRD diffraction peaks from the NiMnSb(111), NiMnSb(002), and NiMnSb(311) superlattices were observed for the NiMnSb film annealed at 500°C, whereas a weak NiMnSb(111) peak and a NiSb(002) peak are shown in the XRD pattern for the sample deposited at room temperature, which indicates that the as-grown sample has a low structural order. Furthermore, the magnitude of half-metallic feature was investigated by AMR measurement because the AMR effect with a negative sign was reported to be necessary for examining the electronic band structures of HMFs (*26*, *27*). Figure 2 (B and C) shows the AMR effect for the two kinds of samples measured at 10 and 300 K, respectively. The dependence of AMR ratio on the in-plane angle ϕ, where $\phi = 0°$ (90°) represents that magnetization is normal (parallel) to the measuring

[1]Institute for Materials Research, Tohoku University, Sendai 980-8577, Japan. [2]Center for Spintronics Research Network, Tohoku University, Sendai 980-8577, Japan. [3]National Institute for Materials Science (NIMS), Tsukuba 304-0047, Japan. [4]Key Laboratory of Materials Modification by Laser, Ion, and Electron Beams (Ministry of Education), School of Materials Science and Engineering, Dalian University of Technology, Dalian, China. [5]Institut für Physik, Universität Augsburg, 86135 Augsburg, Germany. [6]Institut für Theoretische Physik, Universität Regensburg, 93040 Regensburg, Germany. [7]WPI Advanced Institute for Materials Research, Tohoku University, Sendai 980-8577, Japan. [8]Center for Science and Innovation in Spintronics, Core Research Cluster, Tohoku University, Sendai 980-8577, Japan.
*Corresponding author. Email: wen.zhenchao@nims.go.jp (Z.W.); cosimo.gorini@physik.uni-regensburg.de (C.G.)
†These authors contributed equally to this work.

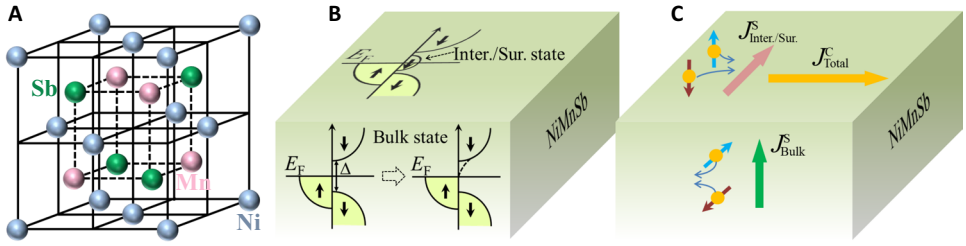

Fig. 1. Schematic illustrations for the NiMnSb crystal and electronic band structures. (**A**) Crystal structure of NiMnSb in the $C1_b$ phase. (**B**) Half-metallic band structure in NiMnSb. The minority band gap closes because of the interaction between electrons and magnons, i.e., the right-hand side illustration of bulk state. The minority band state exists at the interface/surface (Inter./Sur.). (**C**) Spin-charge conversion with interface and bulk contributions. Here, $J^S_{\text{Inter.Sur.}}$ and J^S_{Bulk} represent the spin currents due to interface/surface and bulk, respectively. J^C_{Total} indicates the converted total charge current.

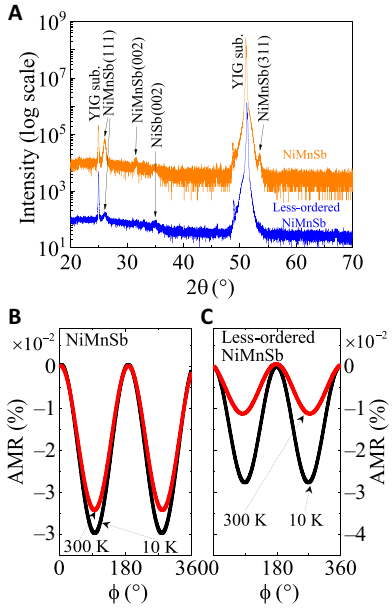

Fig. 2. Structural properties of NiMnSb films and AMR effect in the films. (**A**) Out-of-plane XRD patterns for 20-nm-thick NiMnSb films with two different ordering structures. (**B**) AMR effect for the two kinds of NiMnSb films measured by an in-plane ϕ scan method at a magnetic field of 2 T at 10 and 300 K, respectively.

current, shows a negative sign ($\rho_{0°} > \rho_{90°}$) for the NiMnSb film. The AMR effect at 10 K is much larger than that measured at 300 K, which indicates the reduction of the spin polarization at the high temperature due to thermal excitation. For the less-ordered sample, the AMR effect is smaller than that in the high-ordered sample, which is consistent with the degradation in half-metallicity.

Furthermore, the measurement of spin-charge conversion was carried out by a spin pumping method, as illustrated in Fig. 3A. Ferromagnetic resonance (FMR) is excited in YIG by applying a microwave with an external magnetic field; thus, spin currents are pumped into NiMnSb. Because of the spin-orbit interactions, an electric current is generated by spin-to-charge conversion in NiMnSb, which can be picked up by the electrodes placed on the NiMnSb film. The dependence of electric voltage on temperature was investigated in the temperature range of 10 to 300 K. Note that the FMR absorption spectrum of NiMnSb layer and the electric voltage at the NiMnSb resonance were also observed, and the signals are much smaller than those due to YIG and can be distinct from the separation of resonance field positions of NiMnSb and YIG. The details are shown in the Supplementary Materials. Figure 3B indicates magnetic field dependence of voltage signal measured at 10 and 300 K under a microwave source of 5 GHz and 25 mW. A sign change of the voltage was observed at 10 K. Figure 3C shows detailed spectra for both FMR of YIG (left) and voltage signals in NiMnSb (right) measured at different temperatures. Corresponding to the resonance absorption, voltage signals were observed in the NiMnSb film grown on the YIG substrate. The magnetic field (H_V) at the maximum voltage coincides with the resonance field (H_{FMR}) of FMR absorption, which indicates that the voltage signal originates from the FMR of YIG. In addition, since the NiMnSb is a ferromagnetic material, the anomalous Hall effect (AHE) could appear because of rectification effect (*28*), which may also contribute an electric voltage. To make a quantitative analysis, the observed voltage signals were fitted by the following equation (*29*)

$$V = V_{SC}\frac{\Delta H^2}{(H_{ex}-H_V)^2+\Delta H^2} + V_{AHE}\frac{-2\Delta H(H_{ex}-H_V)}{(H_{ex}-H_V)^2+\Delta H^2} \quad (1)$$

where V_{SC} represents the voltage by spin-charge conversion, V_{AHE} is the contribution from AHE, and ΔH is the full width at half maximum for the voltage signal. Typical fitting results for the measured voltage signals at 10 and 300 K are shown as solid lines in Fig. 3B. It is found that the observed voltage is mainly contributed by spin-charge conversion, where the ratio of V_{SC}/V_{AHE} is obtained to be 12.7 at 300 K (11.9 at 10 K). For the other parameters, the H_V is 1020 Oe at 300 K (886 Oe at 10 K) and the ΔH is 21 Oe at 300 K (28 Oe at 10 K). Note that the parameter values were averaged from the fitting results in negative and positive magnetic field directions.

The dependence of V_{SC} on measuring temperature was further investigated under different microwave conditions and NiMnSb thicknesses. Figure 4A shows the temperature dependence of V_{SC} with varying microwave power of P_{in} = 50, 100, and 200 mW at a fixed microwave frequency of f = 5 GHz for a 20-nm-thick NiMnSb film. It is observed that a sign change of V_{SC} appears at the temperature of T_{cross} ~ 40 K. With further increasing temperature, a marked increase of the amplitude of V_{SC} is observed up to ~150 K. Then, the amplitude of the V_{SC} shows a weak dependence on temperature when the measuring temperature increases to 300 K. The unique feature of the temperature dependence of V_{SC} is regardless of microwave powers. Furthermore, the V_{SC} as a function of temperature was also studied by applying different microwave frequencies of f = 5, 6, and 7 GHz at a fixed microwave power of P_{in} = 25 mW, as shown in Fig. 4B. A similar tendency of temperature dependence of V_{SC} was

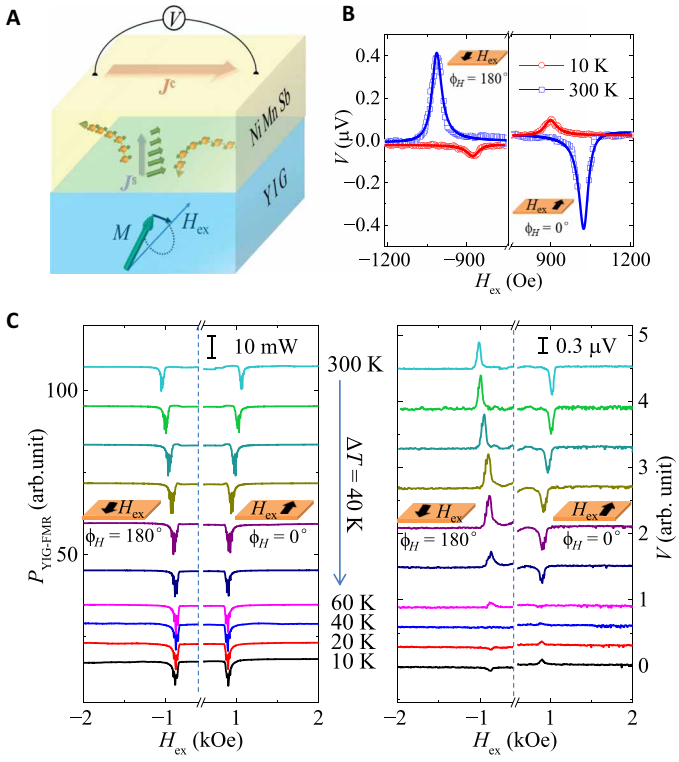

Fig. 3. Voltage measurement with spin pumping. (**A**) Schematic illustration of the YIG/NiMnSb sample with experiment setup carried out in the study. (**B**) Magnetic field dependence of the electronic voltage, *V*, measured at 10 and 300 K. The directions of external magnetic field, H_{ex}, are also indicated by the inset illustrations. The blue and red solid lines are fitting results for the experimental data by Eq. 1. (**C**) FMR spectra in YIG (left) and voltage signals in NiMnSb (right) measured in the temperature range from 10 to 300 K. The applied microwave power and frequency here are 25 mW and 5 GHz, respectively.

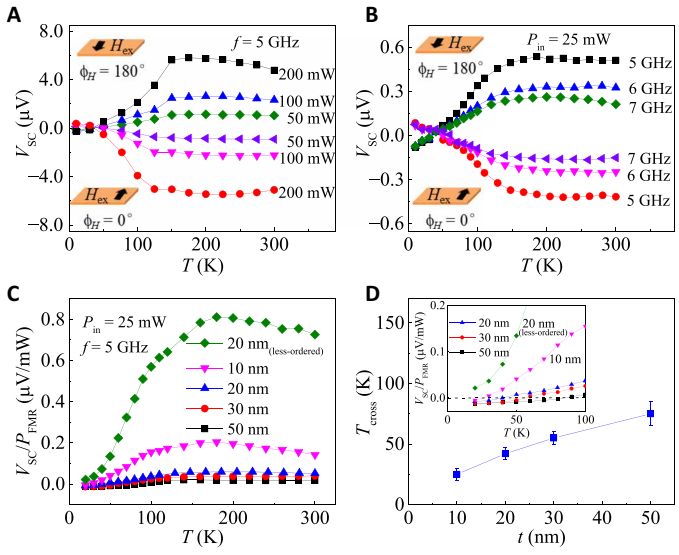

Fig. 4. Temperature dependence of V_{SC} with varying microwave power, microwave frequency, and NiMnSb thickness. (**A**) V_{SC} as a function of temperature measured at different microwave powers of P_{in} = 50, 100, and 200 mW, with the microwave frequency of f = 5 GHz. (**B**) V_{SC} as a function of temperature at different microwave frequencies of f = 5, 6, and 7 GHz with the microwave power of P_{in} = 25 mW. (**C**) Temperature dependence of V_{SC} divided by the amplitude of FMR absorption of YIG for NiMnSb films with the thickness of 10, 20, 30, and 50 nm. The V_{SC} measured in a less-ordered NiMnSb film with the thickness of 20 nm is also shown for comparison. The microwave condition is P_{in} = 25 mW and f = 5 GHz. (**D**) The dependence of cross temperature, T_{cross}, for the sign change of V_{SC} on NiMnSb thickness, *t*. The inset is an enlarged view of (C) in the temperature region below 100 K.

observed at the different frequencies. In addition, the value of T_{cross} for the sign change of V_{SC} remains the same (~40 K) under the different conditions. A reduction of amplitude of V_{SC} is observed with the increase of microwave frequency, which is consistent with the previously reported relationship between V_{SC} and f (*30*). Moreover, V_{SC} was investigated in NiMnSb films with different film thicknesses. To make a quantitative comparison, the measured V_{SC} was divided by the corresponding amplitude of FMR absorption, P_{FMR}, of the YIG. Figure 4C shows the V_{SC}/P_{FMR} as a function of temperature for the NiMnSb films with the thicknesses of t = 10, 20, 30, and 50 nm and for a less-ordered NiMnSb film with the thickness of 20 nm. It is found that the less-ordered sample shows a large V_{SC} in the entire temperature range, which could be attributed to the existence of more scattering centers due to the low structural order in the sample. In addition, the magnitude of V_{SC} decreases with increasing NiMnSb thickness from 10 to 50 nm. Apart from the magnitude of V_{SC}, the temperature dependence shows a similar trend for all the samples regardless of thickness and ordering structure. Nevertheless, the temperature of T_{cross} for the sign change of V_{SC} reveals a distinct dependence on the film thickness, as shown in Fig. 4D. An enlarged view of Fig. 4C in the temperature region of below 100 K is also shown in the inset of Fig. 4D. The T_{cross} increases from 25 to 75 K with the increase of NiMnSb thickness from 10 to 50 nm. The less-ordered sample shows no sign change of V_{SC} in the measuring temperature range. Furthermore, we note that Ciccarelli *et al.* (*25*) reported a dependence of crystal symmetries on spin-orbit torques in single-crystalline NiMnSb films. The angular dependence of spin-charge conversion has also been investigated for one of the current polycrystalline samples (20-nm-thick NiMnSb film on YIG substrate). Details are shown in the Supplementary Materials. We observe that the angular dependence is different from that of the single-crystalline NiMnSb reported by Ciccarelli *et al.* (*25*). According to a review paper for spin pumping (*31*), the angular dependence for the spin pumping measurement under in-plane magnetic field with in-plane radio frequency field excitation usually follows the $\cos^3\phi_H$ function. By using this function, our experimental results are fairly fitted. Therefore, an anisotropy of spin-charge conversion due to crystal symmetries is not likely to be present in our polycrystalline NiMnSb samples.

DISCUSSION

In the following, we theoretically discuss and analyze the observed voltage due to spin-charge conversion, as well as its temperature dependence. Technical details are presented in the Supplementary Materials. First, by considering the low-temperature regime, the experimental data show a nonvanishing voltage V_0 when approaching zero temperature. At T = 0 K, it is, however, impossible to inject a pure spin current, a net spin current in the absence of any charge current, into a perfect HMF: Pumping such a current requires establishing an equal-in-magnitude and opposite-in-sign chemical potential imbalance for two different spin species (*32*), while a perfect

HMF has only one available. Since the pumping source is YIG, a ferrimagnetic insulator (no carriers available for spurious charge injection), this signal must be related to a spin-orbit active interface region, expected to be about 1 to 2 nm, where the perfect half-metallicity is known to be degraded (*17*–*22*). Very likely, the interface exhibits a Rashba-like spin-orbit coupling due to structural inversion asymmetry (*33*). The voltage at $T = 0$ K is then attributed to the spin-galvanic (or inverse Edelstein) effect (*34*–*36*) and to the intrinsically dominated case given by

$$V_0 = -\frac{2m\alpha L}{en\hbar} j^s \tag{2}$$

where $e = |e|$ is the elementary charge, L is the sample length, and j^s is the (three-dimensional) spin current density generated by YIG. Furthermore, α is the Rashba coefficient, m is the effective electron mass, and n is the (two-dimensional) particle density of the interface region, respectively. We note, in passing, that interfacial Rashba-like mechanisms do play a determining role in different setups where structural inversion symmetry is broken (*36*–*40*). Thus, it appears reasonable to consider a minimal Rashba-like model, with the result given in Eq. 2. Additional evidence for the interfacial character of the $T = 0$ signal is its independence of the NiMnSb thickness.

Second, at finite temperatures $T > 0$ K, even perfectly half-metallic bulk NiMnSb is capable of absorbing a pure spin current. This is because electron-magnon (spin flip) scattering yields a finite density of states (DOS) for the minority band of NiMnSb (*16*, *41*–*46*)

$$\mathcal{N}^{\downarrow}(\epsilon_F) \approx \mathcal{N}^{\uparrow}(\epsilon_F)\left(\frac{T}{T^*}\right)^{3/2} \tag{3}$$

where $\mathcal{N}^{\uparrow}$ and $\mathcal{N}^{\downarrow}$ are the majority (↑) and minority (↓) DOS, respectively, while $T^* \sim 10^3$ K is a characteristic temperature corresponding to the magnon energy at the boundary of the Stoner continuum. The resulting absorbed spin current $j^s_{\mathrm{eff}}(T)$ is

$$j^s_{\mathrm{eff}}(T) \approx \frac{\mathcal{N}^{\downarrow}(\epsilon_F)}{\mathcal{N}^{\uparrow}(\epsilon_F)} j^s \approx \left(\frac{T}{T^*}\right)^{\frac{3}{2}} j^s \tag{4}$$

The spin current $j^s_{\mathrm{eff}}(T)$ is then converted to a transverse voltage via the inverse spin Hall effect in bulk NiMnSb due to, e.g., extrinsic effects like side-jump and skew scattering with impurities and phonons, yielding

$$V_{\mathrm{HMF}} = \frac{e\rho\theta_{\mathrm{sH}}\lambda_{\mathrm{sd}}L}{2d}\tanh\left(\frac{d}{2\lambda_{\mathrm{sd}}}\right) j^s_{\mathrm{eff}} \tag{5}$$

Here d, θ_{sH}, and ρ are the thickness, spin Hall angle, and (three-dimensional) resistivity of the sample, respectively. Note that ab initio studies show no evidence for spin-orbit splitting of NiMnSb bands at the Fermi level (*17*); therefore, we neglect intrinsic effects. Thus, the total voltage due to spin-charge conversion is the sum of the interface and bulk magnon-induced contributions

$$V_{\mathrm{SC}}(T) = V_0 + V_{\mathrm{HMF}}(T) \tag{6}$$

The interfacial spin-charge conversion is taken to be T independent (V_0 = constant) as a consequence of the following: (i) It is of structural nature and not magnon limited; (ii) As shown by the experimental data, $|V_0| \ll |V_{\mathrm{HMF}}(T \gtrsim 100\ \mathrm{K})|$ so that its possible T dependence is irrelevant for the following analysis. Notice, however, that the condition $|V_0| \ll |V_{\mathrm{HMF}}(T \gtrsim 100\ \mathrm{K})|$ approaches breakdown in the thicker 50-nm sample (see discussion below). The thickness-dependent crossing temperature can already be qualitatively explained: Assuming that $d \gg \lambda_{\mathrm{sd}}$ and $V_{\mathrm{HMF}} \approx$ constant > 0 in the high-temperature region, an increasing thickness d compresses the total $V_{\mathrm{HMF}}(T) \sim 1/d$ curve (see Eq. 5). For $V_0 < 0$ (see inset of Fig. 4D), the crossing temperature thus increases with increasing thickness as sketched in Fig. 5. Regarding the sign of V_0, there are some methods that attempt to give estimates for the Rashba coefficient α via the work functions (*47*) or on the basis of the **k·p** theory (*48*). However, in the absence of any precise microscopic understanding of the YIG/NiMnSb interface, these are of limited reliability, so we take the offset voltage as a parameter and, indeed, find it, from comparison with experiment, to be negative.

In addition to the temperature-dependent effective pumping spin current (Eq. 4), the resistivity ρ, spin Hall angle θ_{sH}, and spin diffusion length λ_{sd}, all appearing in Eq. 5, are temperature dependent as well. Let us start from the latter

$$\lambda_{\mathrm{sd}} = \sqrt{\frac{2D_{\uparrow}D_{\downarrow}\tau_s}{D_{\uparrow}+D_{\downarrow}}} \tag{7}$$

The spin diffusion length depends on the diffusion constants of the majority and minority spin electrons, $D_{\uparrow}$ and $D_{\downarrow}$, respectively, and on the spin-flip relaxation time τ_s. Assuming that $D_{\uparrow} \gg D_{\downarrow}$, and $D_{\downarrow}$ and τ_s are proportional to $1/\mathcal{N}^{\downarrow}$, the spin diffusion length is estimated as

$$\lambda_{\mathrm{sd}} \approx \sqrt{2D_{\downarrow}\tau_s} \sim \left(\frac{T^*}{T}\right)^{\frac{3}{2}} \tag{8}$$

From Eq. 4, note that the product $\lambda_{\mathrm{sd}} j^s_{\mathrm{eff}}$ in Eq. 5 is independent of temperature.

The spin Hall angle can be separated into majority and minority band contributions, $\theta^{\uparrow}_{\mathrm{sH}}$ and $\theta^{\downarrow}_{\mathrm{sH}}$, respectively, and the same is done for the corresponding spin Hall conductivities, $\sigma^{\uparrow}_{\mathrm{sH}}$ and $\sigma^{\downarrow}_{\mathrm{sH}}$. According to (*16*), $\sigma^{\downarrow}_{\mathrm{sH}}$ is negligible compared to $\sigma^{\uparrow}_{\mathrm{sH}}$ so that $\theta_{\mathrm{sH}} \approx \theta^{\uparrow}_{\mathrm{sH}}$. The T dependence of the spin Hall angle of a metallic system was discussed by Karnad *et al.* (*49*), where intrinsic spin-orbit coupling and skew scattering dominate and the nonmonotonic T dependence of the spin Hall signal cannot be deduced on the basis of the standard scaling theory (*50*). Here, we follow this treatment, introducing, however, in addition to skew scattering, a phenomenological contribution, which is lifetime and, thus, temperature independent. Its microscopic origin could be extrinsic, e.g., due to side jump (*51*), or intrinsic, e.g., arising from Fermi sea contributions of the kind relevant for the AHE

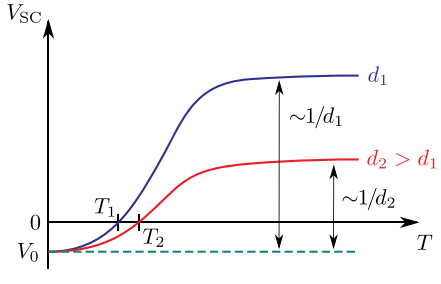

Fig. 5. Sketch of the voltage due to spin-charge conversion as a function of temperature. There are two thicknesses, d_1 (blue) and d_2 (red) ($d_2 > d_1$), with the crossing temperatures T_1 and T_2 ($T_2 > T_1$), respectively. The green dashed line is the interfacial contribution V_0.

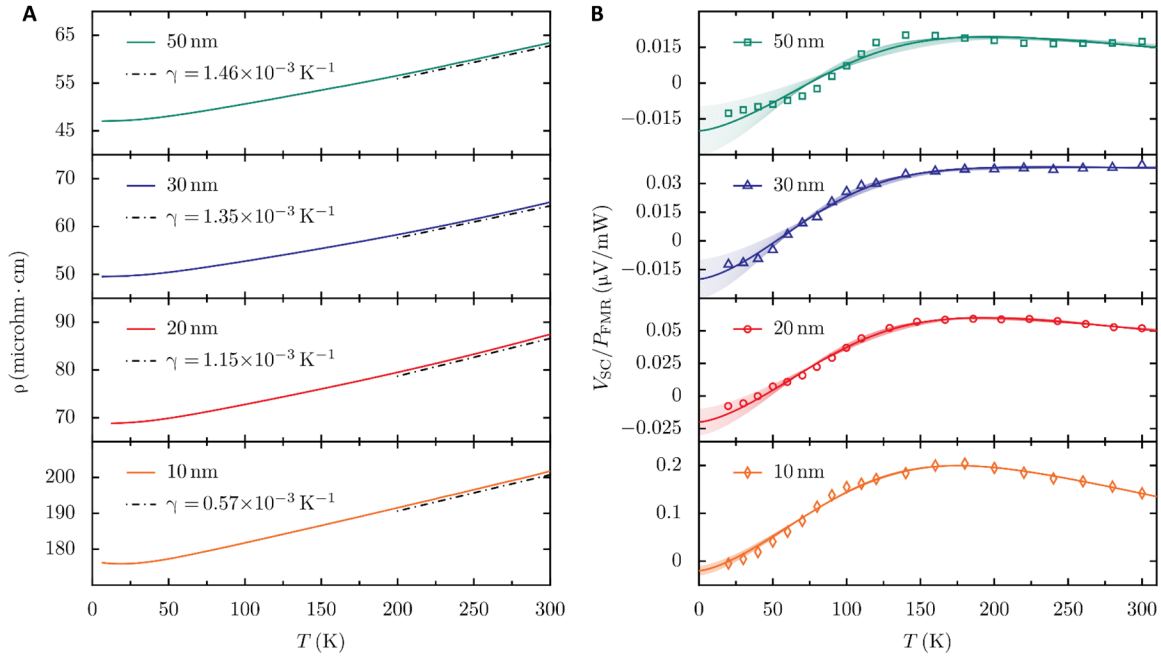

Fig. 6. Resistivity of NiMnSb films and the voltage due to spin-charge conversion as a function of temperature. (**A**) The dependence of the resistivity on temperature for the NiMnSb films with d = 10, 20, 30, and 50 nm. The linear T dependence ($\sim\gamma T$) in the high-temperature regime is indicated by a dash-dotted line with the respective value of γ for each thickness. (**B**) The voltage signal divided by the amplitude of FMR absorption of YIG against the temperature for the various thicknesses of the NiMnSb layer. The symbols represent the experimental data, and the solid line shows their fitted curve with the use of Eq. 9, with V_0/P_{FMR} = −0.02 μV/mW, respectively. The shaded areas show the range of fitting curves for −0.03 μV/mW < V_0/P_{FMR} < −0.01 μV/mW.

(*52*, *53*). This phenomenological contribution to the corresponding spin Hall conductivity is denoted by σ^{*}_{sH}, while the skew scattering contribution at temperature T is denoted, as usual, by $\sigma^{ss,T}_{sH}$. Last, the resistivity $\rho(T)$ of our samples is known and appears in Fig. 6A. The overall voltage is thus described by

$$V_{SC}(T) = V_0 + \frac{AP_{FMR}}{d}(1 + BT)\tanh(d\mathrm{C}T^{3/2}) \qquad (9)$$

which serves as a fitting equation with the parameters A, B, and C to the experimental data (Fig. 6B), where V_0/P_{FMR} = −0.02 μV/mW (see details in the Supplementary Materials). Notice that this is not a three-parameter fit, since A, B, and C are not independent. B is further constrained by the measured resistivity values via the known parameter γ (see Fig. 6A and details in the Supplementary Materials). The parameter B allows us to extract the ratio between the scattering-independent and the skew scattering contributions at zero temperature (see Table 1). From C, we obtain spin diffusion lengths for each layer thickness. As shown in Table 1, λ_{sd} at room temperature has reasonable values in the range of nanometers.

Equation 9 fits the experimental data of the 10-, 20-, 30-, and 50-nm-thick samples very well. The slightly reduced accuracy in the case of 50-nm data can be explained by the decrease of the bulk contribution, $V_{HMF} \sim 1/d$ according to Eq. 5. Particularly, $|V_{HMF}| \approx |V_0|$ even at high temperature for the 50-nm sample so that the T dependence of the interfacial contribution V_0 could play a considerable role. The overall good match between data and fitted curves supports our argument that the total signal is the sum of (i) a mostly temperature-independent interfacial contribution V_0 and (ii) a thickness-dependent bulk, one mainly limited by minority states due to thermally excited magnons with a spin diffusion length of $\sim T^{-3/2}$. In addition, the sign change of V_{SC} was not observed for the less-ordered sample in the measurement temperature range, which indicates that the bulk contribution is much larger than the interface contribution even at low temperatures due to the degraded half-metallicity.

Table 1. Spin diffusion length and ratio $\sigma^{*}_{sH}/\sigma^{ss,0}_{sH}$. The spin diffusion length at room temperature (300 K) and the ratio $\sigma^{*}_{sH}/\sigma^{ss,0}_{sH}$ for the various thicknesses of the NiMnSb films are obtained by the fit of Eq. 9 to the experimental data as shown in Fig. 6B for V_0/P_{FMR} = −0.03, −0.02, and −0.01 μV/mW from left to right. Note that σ^{*}_{sH} is temperature independent by definition and that $\sigma^{ss,0}_{sH}$ denotes the zero-temperature value of the skew scattering contribution.

d	λ_{sd} (300 K) (nm)			$\sigma^{*}_{sH}/\sigma^{ss,0}_{sH}$		
50 nm	9.47	14.03	19.65	−0.16	−0.27	−0.29
30 nm	4.74	6.32	8.31	0.09	−0.05	−0.12
20 nm	4.21	5.48	7.27	−0.23	−0.32	−0.39
10 nm	2.82	3.07	3.37	−0.60	−0.62	−0.63

In conclusion, the spin-charge conversion in NiMnSb alloy films was investigated through the injection of spin current from YIG by spin pumping. It was observed that the voltage due to spin-charge conversion showed an unusual temperature dependence and a sign change at low temperature depending on film thickness and ordering structure. The temperature-dependent behavior of the voltage in the NiMnSb films was further analyzed by the spin-charge conversion

contributed by interface and bulk effects. This study could be of significance for the understanding of bulk and interface contributions for the spin-charge conversion in ferromagnetic materials, especially in HMFs.

MATERIALS AND METHODS

The NiMnSb alloy films were deposited on YIG substrates by a cosputtering method from Ni and MnSb targets in an ultrahigh vacuum magnetron sputtering system with a base pressure of ~1×10^{-7} Pa. AlO_x (1.5 nm thick) was subsequently deposited on the NiMnSb films for protection. The stoichiometric composition of the NiMnSb films was confirmed to be $Ni_{1.01}Mn_{0.98}Sb_{1.01}$ by inductively coupled plasma analysis. The samples with high ordering structure were deposited at a substrate temperature of 500°C, while the sample with low order was grown at room temperature. The structural properties of NiMnSb films were characterized by XRD with Cu Kα radiation (λ = 0.15418 nm). AMR effect was measured at 10 and 300 K by a physical properties measurement system (PPMS). The YIG-substrate/NiMnSb device was placed on a coplanar waveguide where the microwave was applied. Two-terminal electrodes were attached on the device for measuring the voltage. The magnetic field was applied in the plane of the films and perpendicular to the direction across the two electrodes. The power of the microwave was varied from 25 to 200 mW, and the frequency was changed from 5 to 7 GHz. The voltage signal was detected by using lock-in techniques, and the voltage measurement was performed in PPMS at low and room temperatures.

SUPPLEMENTARY MATERIALS

Supplementary material for this article is available at http://advances.sciencemag.org/cgi/content/full/5/12/eaaw9337/DC1

Section S1. Experimental results on the FMR spectrum of NiMnSb and the voltage signals due to the NiMnSb resonance and angular dependence of voltage signal by spin-charge conversion

Section S2. Technical details of the theory of the voltage due to spin-charge conversion

Fig. S1. Typical FMR spectra and voltage signals in the YIG/NiMnSb (20 nm) sample.

Fig. S2. Angular dependence of voltage signal by spin-charge conversion.

References (*54*–*58*)

REFERENCES AND NOTES

1. Y. K. Kato, R. C. Myers, A. C. Gossard, D. D. Awschalom, Observation of the spin Hall effect in semiconductors. *Science* **306**, 1910–1913 (2004).
2. S. O. Valenzuela, M. Tinkham, Direct electronic measurement of the spin Hall effect. *Nature* **442**, 176–179 (2006).
3. T. Seki, Y. Hasegawa, S. Mitani, S. Takahashi, H. Imamura, S. Maekawa, J. Nitta, K. Takanashi, Giant spin Hall effect in perpendicularly spin-polarized FePt/Au devices. *Nat. Mater.* **7**, 125–129 (2008).
4. L. Liu, C.-F. Pai, Y. Li, H. W. Tseng, D. C. Ralph, R. A. Buhrman, Spin-torque switching with the giant spin hall effect of tantalum. *Science* **336**, 555–558 (2012).
5. A. R. Mellnik, J. S. Lee, A. Richardella, J. L. Grab, P. J. Mintun, M. H. Fischer, A. Vaezi, A. Manchon, E.-A. Kim, N. Samarth, D. C. Ralph, Spin-transfer torque generated by a topological insulator. *Nature* **511**, 449–451 (2014).
6. Y. Fan, P. Upadhyaya, X. Kou, M. Lang, S. Takei, Z. Wang, J. Tang, L. He, L.-T. Chang, M. Montazeri, G. Yu, W. Jiang, T. Nie, R. N. Schwartz, Y. Tserkovnyak, K. L. Wang, Magnetization switching through giant spin–orbit torque in a magnetically doped topological insulator heterostructure. *Nat. Mater.* **13**, 699–704 (2014).
7. Y. Wang, D. Zhu, Y. Wu, Y. Yang, J. Yu, R. Ramaswamy, R. Mishra, S. Shi, M. Elyasi, K.-L. Teo, Y. Wu, H. Yang, Room temperature magnetization switching in topological insulator-ferromagnet heterostructures by spin-orbit torques. *Nat. Commun.* **8**, 1364 (2017).
8. S. Iihama, T. Taniguchi, K. Yakushiji, A. Fukushima, Y. Shiota, S. Tsunegi, R. Hiramatsu, S. Yuasa, Y. Suzuki, H. Kubota, Spin-transfer torque induced by the spin anomalous Hall effect. *Nat. Electron.* **1**, 120–123 (2018).
9. S.-h. C. Baek, V. P. Amin, Y.-W. Oh, G. Go, S.-J. Lee, G.-H. Lee, K.-J. Kim, M. D. Stiles, B.-G. Park, K.-J. Lee, Spin currents and spin–orbit torques in ferromagnetic trilayers. *Nat. Mater.* **17**, 509–513 (2018).
10. B. F. Miao, S. Y. Huang, D. Qu, C. L. Chien, Inverse spin hall effect in a ferromagnetic metal. *Phys. Rev. Lett.* **111**, 066602 (2013).
11. H. Wang, C. Du, P. Chris Hammel, F. Yang, Spin current and inverse spin Hall effect in ferromagnetic metals probed by $Y_3Fe_5O_{12}$-based spin pumping. *Appl. Phys. Lett.* **104**, 202405 (2014).
12. T. Seki, K.-i. Uchida, T. Kikkawa, Z. Qiu, E. Saitoh, K. Takanashi, Observation of inverse spin Hall effect in ferromagnetic FePt alloys using spin Seebeck effect. *Appl. Phys. Lett.* **107**, 092401 (2015).
13. R. A. De Groot, F. M. Mueller, P. G. Van Engen, K. H. J. Buschow, New class of materials: Half-metallic ferromagnets. *Phys. Rev. Lett.* **50**, 2024–2027 (1983).
14. M. Jourdan, J. Minár, J. Braun, A. Kronenberg, S. Chadov, B. Balke, A. Gloskovskii, M. Kolbe, H. J. Elmers, G. Schönhense, H. Ebert, C. Felser, M. Kläui, Direct observation of half-metallicity in the Heusler compound Co_2MnSi. *Nat. Commun.* **5**, 3974 (2014).
15. H.-x. Liu, T. Kawami, K. Moges, T. Uemura, M. Yamamoto, F. Shi, P. M. Voyles, Influence of film composition in quaternary Heusler alloy Co_2(Mn,Fe)Si thin films on tunnelling magnetoresistance of Co_2(Mn,Fe)Si/MgO-based magnetic tunnel junctions. *J. Phys. D. Appl. Phys.* **48**, 164001 (2015).
16. Y. Ohnuma, M. Matsuo, S. Maekawa, Spin transport in half-metallic ferromagnets. *Phys. Rev. B* **94**, 184405 (2016).
17. M. I. Katsnelson, V. Y. Irkhin, L. Chioncel, A. I. Lichtenstein, R. A. de Groot, Half-metallic ferromagnets: From band structure to many-body effects. *Rev. Mod. Phys.* **80**, 315–378 (2008).
18. G. L. Bona, F. Meier, M. Taborelli, E. Bucher, P. H. Schmidt, Spin polarized photoemission from NiMnSb. *Solid State Commun.* **56**, 391–394 (1985).
19. R. J. Soulen, J. M. Byers, M. S. Osofsky, B. Nadgorny, T. Ambrose, S. F. Cheng, P. R. Broussard, C. T. Tanaka, J. Nowak, J. S. Moodera, A. Barry, J. M. D. Coey, Measuring the spin polarization of a metal with a superconducting point contact. *Science* **282**, 85–88 (1998).
20. C. T. Tanaka, J. Nowak, J. S. Moodera, Spin-polarized tunneling in a half-metallic ferromagnet. *J. Appl. Phys.* **86**, 6239–6242 (1999).
21. G. A. de Wijs, R. A. de Groot, Towards 100% spin-polarized charge-injection: The half-metallic NiMnSb/CdS interface. *Phys. Rev. B* **64**, 020402 (2001).
22. I. Galanakis, Surface properties of the half-and full-Heusler alloys. *J. Phys. Condens. Matter* **14**, 6329–6340 (2002).
23. Z. Wen, T. Kubota, T. Yamamoto, K. Takanashi, Fully epitaxial $C1_b$-type NiMnSb half-Heusler alloy films for current-perpendicular-to-plane giant magnetoresistance devices with a Ag spacer. *Sci. Rep.* **5**, 18387 (2015).
24. Z. Wen, T. Kubota, T. Yamamoto, K. Takanashi, Enhanced current-perpendicular-to-plane giant magnetoresistance effect in half-metallic NiMnSb based nanojunctions with multiple Ag spacers. *Appl. Phys. Lett.* **108**, 232406 (2016).
25. C. Ciccarelli, L. Anderson, V. Tshitoyan, A. J. Ferguson, F. Gerhard, C. Gould, L. W. Molenkamp, J. Gayles, J. Železný, L. Šmejkal, Z. Yuan, J. Sinova, F. Freimuth, T. Jungwirth, Room-temperature spin–orbit torque in NiMnSb. *Nat. Phys.* **12**, 855–860 (2016).
26. Y. Sakuraba, S. Kokado, Y. Hirayama, T. Furubayashi, H. Sukegawa, S. Li, Y. K. Takahashi, K. Hono, Quantitative analysis of anisotropic magnetoresistance in Co_2MnZ and Co_2FeZ epitaxial thin films: A facile way to investigate spin-polarization in half-metallic Heusler compounds. *Appl. Phys. Lett.* **104**, 172407 (2014).
27. S. Kokado, M. Tsunoda, K. Harigaya, A. Sakuma, Anisotropic magnetoresistance effects in Fe, Co, Ni, Fe_4N, and half-metallic ferromagnet: A systematic analysis. *J. Phys. Soc. Jpn.* **81**, 024705 (2012).
28. L. Bai, P. Hyde, Y. S. Gui, C. M. Hu, V. Vlaminck, J. E. Pearson, S. D. Bader, A. Hoffmann, Universal method for separating spin pumping from spin rectification voltage of ferromagnetic resonance. *Phys. Rev. Lett.* **111**, 217602 (2013).
29. E. Saitoh, M. Ueda, H. Miyajima, G. Tatara, Conversion of spin current into charge current at room temperature: Inverse spin-Hall effect. *Appl. Phys. Lett.* **88**, 182509 (2006).
30. H. L. Wang, C. H. Du, Y. Pu, R. Adur, P. C. Hammel, F. Y. Yang, Scaling of spin Hall angle in 3d, 4d, and 5d metals from $Y_3Fe_5O_{12}$/metal spin pumping. *Phys. Rev. Lett.* **112**, 197201 (2014).
31. R. Iguchi, E. Saitoh, Measurement of spin pumping voltage separated from extrinsic microwave effects. *J. Phys. Soc. Jpn.* **86**, 011003 (2017).
32. Y. Tserkovnyak, A. Brataas, G. E. W. Bauer, B. I. Halperin, Nonlocal magnetization dynamics in ferromagnetic heterostructures. *Rev. Mod. Phys.* **77**, 1375–1421 (2005).
33. The bulk crystal structure of NiMnSb should also yield a linear-in-momentum spin-orbit term according to Dresselhaus (*25*). The precise angular dependence of the spin-orbit field is, however, irrelevant for our discussion, and we limit ourselves to a Rashba term for definiteness' sake.
34. S. D. Ganichev, E. L. Ivchenko, V. V. Bel'kov, S. A. Tarasenko, M. Sollinger, D. Weiss, W. Wegscheider, W. Prettl, Spin-galvanic effect. *Nature* **417**, 153–156 (2002).
35. K. Shen, G. Vignale, R. Raimondi, Microscopic theory of the inverse Edelstein effect. *Phys. Rev. Lett.* **112**, 096601 (2014).

36. J. C. R. Sánchez, L. Vila, G. Desfonds, S. Gambarelli, J. P. Attané, J. M. D. Teresa, C. Magén, A. Fert, Spin-to-charge conversion using Rashba coupling at the interface between non-magnetic materials. *Nat. Commun.* **4**, 2944 (2013).
37. J. Ryu, M. Kohda, J. Nitta, Observation of the D'yakonov-Perel' spin relaxation in single-crystalline Pt thin films. *Phys. Rev. Lett.* **116**, 256802 (2016).
38. L. Zhou, H. Song, K. Liu, Z. Luan, P. Wang, L. Sun, S. Jiang, H. Xiang, Y. Chen, J. Du, H. Ding, K. Xia, J. Xiao, D. Wu, Observation of spin-orbit magnetoresistance in metallic thin films on magnetic insulators. *Sci. Adv.* **4**, eaao3318 (2018).
39. A. M. Shikin, A. Varykhalov, G. V. Prudnikova, D. Usachov, V. K. Adamchuk, Y. Yamada, J. D. Riley, O. Rader, Origin of spin-orbit splitting for monolayers of Au and Ag on W(110) and Mo(110). *Phys. Rev. Lett.* **100**, 057601 (2008).
40. A. M. Shikin, A. A. Rybkina, A. S. Korshunov, Y. B. Kudasov, N. V. Frolova, A. G. Rybkin, D. Marchenko, J. Sánchez-Barriga, A. Varykhalov, O. Rader, Induced Rashba splitting of electronic states in monolayers of Au, Cu on a W(110) substrate. *New J. Phys.* **15**, 095005 (2013).
41. J. A. Hertz, D. M. Edwards, Electron-magnon interactions in itinerant ferromagnetism. I. Formal theory. *J. Phys. F* **3**, 2174 (1973).
42. D. M. Edwards, J. A. Hertz, Electron-magnon interactions in itinerant ferromagnetism. II. Strong ferromagnetism. *J. Phys. F* **3**, 2191 (1973).
43. L. Chioncel, M. I. Katsnelson, R. A. de Groot, A. I. Lichtenstein, Nonquasiparticle states in the half-metallic ferromagnet NiMnSb. *Phys. Rev. B* **68**, 144425 (2003).
44. S. Chadov, J. Minár, H. Ebert, A. Perlov, L. Chioncel, M. I. Katsnelson, A. I. Lichtenstein, Influence of correlation effects on the magneto-optical properties of the half-metallic ferromagnet NiMnSb. *Phys. Rev. B* **74**, 140411 (2006).
45. V. Y. Irkhin, M. I. Katsnelson, Spin-polarized scanning tunneling microscopy of half-metallic ferromagnets: Nonquasiparticle contributions. *Phys. Rev. B* **73**, 104429 (2006).
46. H. Allmaier, L. Chioncel, E. Arrigoni, M. I. Katsnelson, A. I. Lichtenstein, Half-metallicity in NiMnSb: A variational cluster approach with *ab initio* parameters. *Phys. Rev. B* **81**, 054422 (2010).
47. R. Ramaswamy, X. Qiu, T. Dutta, S. D. Pollard, H. Yang, Hf thickness dependence of spin-orbit torques in Hf/CoFeB/MgO heterostructures. *Appl. Phys. Lett.* **108**, 202406 (2016).
48. E. Simon, A. Szilva, B. Ujfalussy, B. Lazarovits, G. Zarand, L. Szunyogh, Anisotropic Rashba splitting of surface states from the admixture of bulk states: Relativistic *ab initio* calculations and k · p perturbation theory. *Phys. Rev. B* **81**, 235438 (2010).
49. G. V. Karnad, C. Gorini, K. Lee, T. Schulz, R. Lo Conte, A. W. J. Wells, D.-S. Han, K. Shahbazi, J.-S. Kim, T. A. Moore, H. J. M. Swagten, U. Eckern, R. Raimondi, M. Kläui, Evidence for phonon skew scattering in the spin Hall effect of platinum. *Phys. Rev. B* **97**, 100405 (2018).
50. Y. Li, N. Kanazawa, X. Z. Yu, A. Tsukazaki, M. Kawasaki, M. Ichikawa, X. F. Jin, F. Kagawa, Y. Tokura, Robust formation of skyrmions and topological hall effect anomaly in epitaxial thin films of MnSi. *Phys. Rev. Lett.* **110**, 117202 (2013).
51. G. Vignale, Ten years of spin hall effect. *J. Supercond. Nov. Magn.* **23**, 3–10 (2010).
52. N. Nagaosa, J. Sinova, S. Onoda, A. H. MacDonald, N. P. Ong, Anomalous Hall effect. *Rev. Mod. Phys.* **82**, 1539–1592 (2010).
53. S. Onoda, N. Sugimoto, N. Nagaosa, Quantum transport theory of anomalous electric, thermoelectric, and thermal Hall effects in ferromagnets. *Phys. Rev. B* **77**, 165103 (2008).
54. Z. Qiu, J. Li, D. Hou, E. Arenholz, A. T. N'Diaye, A. Tan, K. I. Uchida, K. Sato, S. Okamoto, Y. Tserkovnyak, Z. Q. Qiu, E. Saitoh, Spin-current probe for phase transition in an insulator. *Nat. Commun.* **7**, 12670 (2016).
55. D. Hou, Z. Qiu, J. Barker, K. Sato, K. Yamamoto, S. Vélez, J. M. Gomez-Perez, L. E. Hueso, F. Casanova, E. Saitoh, Tunable sign change of spin Hall magnetoresistance in Pt/NiO/YIG structures. *Phys. Rev. Lett.* **118**, 147202 (2017).
56. P. Schwab, R. Raimondi, C. Gorini, Inverse spin Hall effect and anomalous Hall effect in a two-dimensional electron gas. *Europhys. Lett.* **90**, 67004 (2010).
57. C. Gorini, U. Eckern, R. Raimondi, Spin Hall effects due to phonon skew scattering. *Phys. Rev. Lett.* **115**, 076602 (2015).
58. C. N. Borca, T. Komesu, H. Jeong, P. A. Dowben, D. Ristoiu, C. Hordequin, J. Pierre, J. P. Nozières, Effective surface Debye temperature for NiMnSb(100) epitaxial films. *Appl. Phys. Lett.* **77**, 88–90 (2000).

Acknowledgments: We thank S. Maekawa, Y. Ohnuma, J. Xiao, V. L. Grigoryan, L. Chioncel, and K. Samwer for fruitful discussions. **Funding:** This work was partially supported by the KAKENHI (S) (no. 18H05246) and Grant-in-Aid for Challenging Research (Exploratory, 18 K19012) from the Japan Society for the Promotion of Science (JSPS), the Inter-University Cooperative Research Program of the Institute for Materials Research, Tohoku University (no. 19 K0042), and the Advanced Storage Research Consortium (ASRC). Z.Q. acknowledges the support from the National Natural Science Foundation of China (grant no. 11874098), LiaoNing Revitalization Talents Program (XLYC1807156), and the Fundamental Research Funds for the Central Universities [DUT17RC(3)073]. S.T., C.G., and U.E. acknowledge the support from the Deutsche Forschungsgemeinschaft (DFG; German Science Foundation) through TRR 80 (project no. 107745057) and SFB 1277 (project no. 314695032). **Author contributions:** K.T. supervised this study. Z.W. and Z.Q. fabricated all the films and measured the samples. Z.W., Z.Q., T.S., D.H., T.K., K.T., and E.S. analyzed the data. S.T., C.G., and U.E. developed the theoretical discussion. All authors discussed the results and prepared the manuscript. **Competing interests:** The authors declare that they have no competing interests. **Data and materials availability:** All data needed to evaluate the conclusions in the paper are present in the paper and/or the Supplementary Materials. Additional data related to this paper may be requested from the authors.

Submitted 12 February 2019
Accepted 28 October 2019
Published 13 December 2019
10.1126/sciadv.aaw9337

Citation: Z. Wen, Z. Qiu, S. Tölle, C. Gorini, T. Seki, D. Hou, T. Kubota, U. Eckern, E. Saitoh, K. Takanashi, Spin-charge conversion in NiMnSb Heusler alloy films. *Sci. Adv.* **5**, eaaw9337 (2019).